

# Millimeter Wave Channel Modeling and Cellular Capacity Evaluation

Mustafa Riza Akdeniz, *Student Member, IEEE*, Yuanpeng Liu, *Student Member, IEEE*, Mathew K. Samimi, *Student Member, IEEE*, Shu Sun, *Student Member, IEEE*, Sundeeep Rangan, *Senior Member, IEEE*, Theodore S. Rappaport, *Fellow, IEEE*, Elza Erkip, *Fellow, IEEE*

**Abstract**—With the severe spectrum shortage in conventional cellular bands, millimeter wave (mmW) frequencies between 30 and 300 GHz have been attracting growing attention as a possible candidate for next-generation micro- and picocellular wireless networks. The mmW bands offer orders of magnitude greater spectrum than current cellular allocations and enable very high-dimensional antenna arrays for further gains via beamforming and spatial multiplexing. This paper uses recent real-world measurements at 28 and 73 GHz in New York City to derive detailed spatial statistical models of the channels and uses these models to provide a realistic assessment of mmW micro- and picocellular networks in a dense urban deployment. Statistical models are derived for key channel parameters including the path loss, number of spatial clusters, angular dispersion and outage. It is found that, even in highly non-line-of-sight environments, strong signals can be detected 100m to 200m from potential cell sites, potentially with multiple clusters to support spatial multiplexing. Moreover, a system simulation based on the models predicts that mmW systems can offer an order of magnitude increase in capacity over current state-of-the-art 4G cellular networks with no increase in cell density from current urban deployments.

**Index Terms**—millimeter wave radio, 3GPP LTE, cellular systems, wireless propagation, 28 GHz, 73 GHz, urban deployments.

## I. INTRODUCTION

The remarkable success of cellular wireless technologies have led to an insatiable demand for mobile data [1], [2]. The UMTS traffic forecasts [3], for example, predicts that by 2020, *daily* mobile traffic will exceed 800 MB per subscriber leading to 130 exabits ( $10^{18}$ ) of data per year for some operators. Keeping pace with this demand will require new technologies that can offer orders of magnitude increases in cellular capacity.

To address this challenge, there has been growing interest in cellular systems based in the so-called *millimeter-wave* (mmW) bands, between 30 and 300 GHz, where the available bandwidths are much wider than today's cellular networks [4]–[9]. The available spectrum at these frequencies can be easily 200 times greater than all cellular allocations today that are

currently largely constrained to the prime RF real estate under 3 GHz [5]. Moreover, the very small wavelengths of mmW signals combined with advances in low-power CMOS RF circuits enable large numbers ( $\geq 32$  elements) of miniaturized antennas to be placed in small dimensions. These multiple antenna systems can be used to form very high gain, electrically steerable arrays, fabricated at the base station, in the skin of a cellphone, or even within a chip [6], [10]–[17]. Given the very wide bandwidths and large numbers of spatial degrees of freedom, it has been speculated that mmW bands will play a significant role in Beyond 4G and 5G cellular systems [8].

However, the development of cellular networks in the mmW bands faces significant technical obstacles and the precise value of mmW systems needs careful assessment. The increase in omnidirectional free space path loss with higher frequencies due to Friis' Law [18], can be more than compensated by a proportional increase in antenna gain with appropriate beamforming. We will, in fact, confirm this property experimentally below. However, a more significant concern is that mmW signals can be severely vulnerable to shadowing resulting in outages, rapidly varying channel conditions and intermittent connectivity. This issue is particularly concerning in cluttered, urban deployments where coverage frequently requires non-line-of-sight (NLOS) links.

In this paper, we use the measurements of mmW outdoor cellular propagation [19]–[24] in 28 and 73 GHz in New York City to derive detailed the first statistical channel models that can be used for proper mmW system evaluation. The models are used to provide an initial assessment of the potential system capacity and outage. The NYC location was selected since it is representative of likely initial deployments of mmW cellular systems due to the high user density. In addition, the urban canyon environment provides a challenging test case for these systems due to the difficulty in establishing line-of-sight (LOS) links – a key concern for mmW cellular.

Although our earlier work has presented some initial analysis of the data in [19]–[23], this work provides much more detailed modeling necessary for cellular system evaluation. In particular, we develop detailed models for the spatial characteristics of the channel and outage probabilities. To obtain these models, several we present new data analysis techniques. In particular, we propose a clustering algorithm that identifies the group of paths in the angular domain from subsampled spatial measurements. The clustering algorithm is based on a  $K$ -means method with additional heuristics to determine the number of clusters. Statistical models are then

This material is based upon work supported by the National Science Foundation under Grants No. 1116589 and 1237821 as well as generous support from Samsung, Nokia Siemens Networks and InterDigital Communications.

M. Akdeniz (email:makden01@students.poly.edu), Y. Liu (email:yliu20@students.poly.edu), M. Samimi (email:mathewsamimi@gmail.com), S. Sun (email:ss7152@nyu.edu), S. Rangan (email:srangan@poly.edu), T. S. Rappaport (email:tsr@nyu.edu) and E. Erkip (email:elza@poly.edu) are with NYU WIRELESS Center, Polytechnic Institute of New York University, Brooklyn, NY.

derived for key cluster parameters including the number of clusters, cluster angular spread and path loss. For the inter-cluster power fractions, we propose a probabilistic model with maximum likelihood (ML) parameter estimation. In addition, while standard 3GPP models such as [25], [26] use probabilistic LOS-NLOS models, we propose to add a third state to explicitly model the possibility of outages.

The key findings from these models are as follows:

- The omnidirectional path loss is approximately 20 to 25 dB higher in the mmW frequencies relative to current cellular frequencies in distances relevant for small cells. However, due to the reduced wavelength, this loss can be completely compensated by a proportional increase in antenna gain with no increase in physical antenna size. Thus, with appropriate beamforming, *locations that are not in outage will not experience any effective increase in path loss and, in fact, the path loss may be decreased.*
- Our measurements indicate that at many locations, energy arrives in clusters from multiple distinct angular directions, presumably through different macro-level scattering or reflection paths. Locations had up to four clusters, with an average of approximately two. The presence of multiple clusters of paths implies that the possibility of both spatial multiplexing and diversity gains.
- Applying the derived channel models to a standard cellular evaluation framework such as [25], we predict that mmW systems can offer at least an order of magnitude increase in system capacity under reasonable assumptions on bandwidth and beamforming. For example, we show that a hypothetical 1GHz bandwidth TDD mmW system with a 100 m cell radii can provide 25 times greater cell throughput than industry reported numbers for a 20+20 MHz FDD LTE system with similar cell density. Moreover, while the LTE capacity numbers included both single and multi-user multi-input multi-output (MIMO), our mmW capacity analysis did not include any spatial multiplexing gains. We provide strong evidence that these spatial multiplexing gains would be significant.
- The system performance appears to be robust to outages provided they are at levels similar or even a little worse than the outages we observed in the NYC measurements. This robustness to outage is very encouraging since outages is one of the key concerns with mmW cellular. However, we also show that should outages be significantly worse than what we observed, the system performance, particularly the cell edge rate, can be greatly impacted.

In addition to the measurement studies above, some of the capacity analysis in this paper appeared in a conference version [27]. The current work provides much more extensive modeling of the channels, more detailed discussions of the beamforming and MIMO characteristics and simulations of features such as outage.

#### A. Prior Measurements

Particularly with the development of 60 GHz LAN and PAN systems, mmW signals have been extensively characterized in

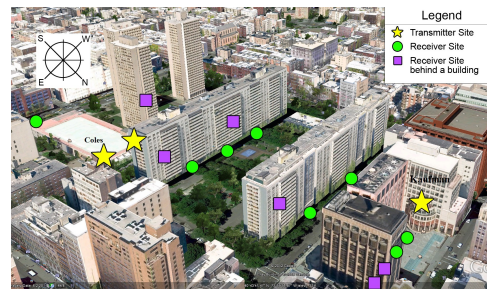


**Fig. 1:** Image from [19] showing typical measurement locations in NYC at 28 GHz. Similar locations were used for 73 GHz.

indoor environments [28]–[34]. However, the propagation of mmW signals in outdoor settings for micro- and picocellular networks is relatively less understood. Due to the lack of actual measured channel data, many earlier studies [4], [7], [35], [36] have thus relied on either analytic models or commercial ray tracing software with various reflection assumptions. Below, we will compare our experimental results with some of these models.

Also, measurements in Local Multipoint Distribution Systems at 28 GHz – the prior system most close to mmW cellular – have been inconclusive: For example, a study [37] found 80% coverage at ranges up to 1–2 km, while [38] claimed that LOS connectivity would be required. Our own previous studies at 38 GHz [39]–[43] found that relatively long-range links (> 300 m) could be established. However, these measurements were performed in an outdoor campus setting with much lower building density and greater opportunities for LOS connectivity than would be found in a typical urban deployment.

## II. MEASUREMENT METHODOLOGY

To assess of mmW propagation in urban environments, our team conducted extensive measurements of 28 and 73 GHz channels in New York City. Details of the measurements can be found in [19]–[21]. Both the 28 and 73 GHz are natural candidates for early mmW deployments. The 28 GHz bands were previously targeted for Local Multipoint Distribution Systems (LMDS) systems and are now an attractive opportunity for initial deployments of mmW cellular given their relatively lower frequency within the mmW range. The E-Band (71-76 GHz and 81-86 GHz) [44] has abundant spectrum and adaptable for dense deployment, and could accommodate further expansion should the lower frequencies become crowded.

To measure the channel characteristics in these frequencies, we emulated microcellular type deployments where transmitters were placed on rooftops 7 and 17 meters (approximately 2 to 5 stories) high and measurements were then made at a number of street level locations up to 500 m from the transmitters (see Fig. 1). To characterize both the bulk path loss and spatial structure of the channels, measurements were performed with highly directional horn antennas (30 dBm RF power, 24.5 dBi gain at both TX and RX sides, and  $\approx 10^\circ$  beamwidths in both the vertical and horizontal planes provided by rotatable horn antennas).

Since transmissions were always made from the rooftop location to the street, in all the reported measurements below, characteristics of the transmitter will be representative of the base station (BS) and characteristics of the receiver will be representative of a mobile, or user equipment (UE). At each transmitter (TX) - receiver (RX) location pair, the azimuth (horizontal) and elevation (vertical) angles of both the transmitter and receiver were swept to first find the direction of the maximal receive power. After this point, power measurements were then made at various angular offsets from the strongest angular locations. In particular, the horizontal angles at both the TX and RX were swept in  $10^\circ$  steps from 0 to  $360^\circ$ . Vertical angles were also sampled, typically within a  $\pm 20^\circ$  range from the horizon in the vertical plane. At each angular sampling point, the channel sounder was used to detect any signal paths. To reject noise, only paths that exceeded a 5 dB SNR threshold were included in the power-delay profile (PDP). Since the channel sounder has a processing gain of 30 dB, only extremely weak paths would not be detected in this system – See [19]–[21] for more details. The power at each angular location is the sum of received powers across all delays (i.e. the sum of the PDP). A location would be considered in *outage* if there were no detected paths across all angular measurements.

### III. CHANNEL MODELING AND PARAMETER ESTIMATION

#### A. Distance-Based Path Loss

We first estimated the total omnidirectional path loss as a function of the TX-RX distance. At each location that was not in outage, the path loss was estimated as

$$PL = P_{TX} - P_{RX} + G_{TX} + G_{RX}, \quad (1)$$

where  $P_{TX}$  is the total transmit power in dBm,  $P_{RX}$  is the total integrated receive power over all the angular directions and  $G_{TX}$  and  $G_{RX}$  are the gains of the horn antennas. For this experiment,  $P_{TX} = 30$  dBm and  $G_{TX} = G_{RX} = 24.5$  dBi. Note that the path loss (1) represents an *isotropic* (omnidirectional, unity antenna gain) value i.e., the difference between the average transmit and receive power seen in a random transmit and receive direction. The path loss thus does not include any beamforming gains obtained by directing the transmitter or receiver correctly – we will discuss the beamforming gains in detail below.

A scatter plot of the path losses at different locations as a function of the TX-RX LOS distance is plotted in Fig. 2. In the measurements in Section II, each location was manually classified as either LOS, where the TX was visible to the RX, or NLOS, where the TX was obstructed. In standard cellular models such as [25], it is common to fit the LOS and NLOS path losses separately.

For the NLOS points, Fig. 2 plots a fit using a standard linear model,

$$PL(d) \text{ [dB]} = \alpha + \beta \log_{10}(d) + \xi, \quad \xi \sim \mathcal{N}(0, \sigma^2), \quad (2)$$

where  $d$  is the distance in meters,  $\alpha$  and  $\beta$  are the least square fits of floating intercept and slope over the measured distances (30 to 200 m), and  $\sigma^2$  is the lognormal shadowing variance.

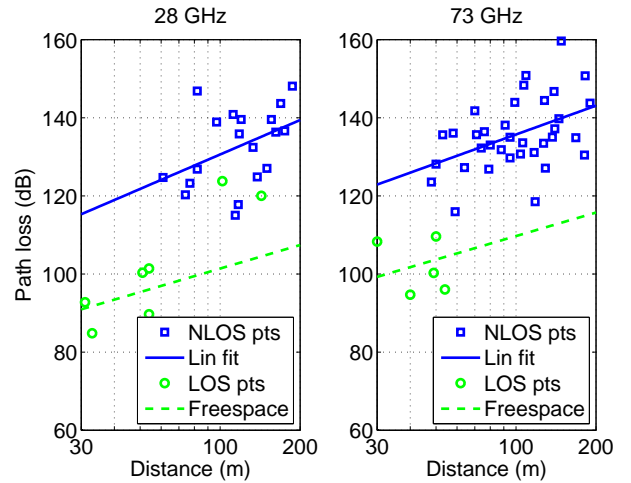


Fig. 2: Scatter plot along with a linear fit of the estimated omnidirectional path losses as a function of the TX-RX separation for 28 and 73 GHz.

The values of  $\alpha$ ,  $\beta$  and  $\sigma^2$  are shown in Table I. To assess the accuracy of the parameter estimates, a standard Cramér-Rao calculation shows that the standard deviation in the median path loss due to noise was  $< 2$  dB over the range of tested distances.

Note that for  $f_c = 73$  GHz, there were two mobile antenna heights in the experiments: 4.02 m (a typical backhaul receiver height) and 2.0 m (a typical model height). The table provides numbers for both a mixture of heights and for the mobile only height. Unless otherwise stated, we will use the mobile only height in all subsequent analysis.

For the LOS points, Fig. 2 shows that the theoretical free space path loss from Friis' Law [18] provides a good fit for the LOS points below 100m. However, at 28 GHz, there are two LOS points at distances greater than 100m where the path loss is not well-fit via a free space propagation model. It is likely that these two points saw higher path losses, since although the TX was visible to the RX, the main path arrived in a NLOS direction. The values for  $\alpha$  and  $\beta$  predicted by Friis' law and the mean-squared error  $\sigma^2$  of the observed data from Friis' Law are shown in Table I.

We should note that these numbers differ somewhat with the values reported in earlier work [19]–[21]. Those works fit the path loss to power measurements for small angular regions. Here, we are fitting the total power over all directions. Also, note that a close-in free space reference path loss model with a fixed leverage point may also be used. Such a fit is equivalent to using the linear model (2) with the additional constraint that  $\alpha + \beta \log_{10}(d_0)$  has some fixed value for some given reference free space distance  $d_0$ . Work in [43] shows that since this close-in free space model has one less free parameter, the model is less sensitive to perturbations in data, with only a slightly greater (e.g. 0.5 dB standard deviation) fitting error. While the analysis below will not use this fixed leverage point model, we point this out to caution against ascribing any physical meaning to the estimated values for  $\alpha$  or  $\beta$  in (2), and understanding that the values are somewhat sensitive to the data and should not be used outside the tested distances.

## B. Spatial Cluster Detection

To characterize the spatial pattern of the antenna, we follow a standard model along the lines of the 3GPP / ITU MIMO specification [25], [26]. In the 3GPP / ITU MIMO model, the channel is assumed to be composed of a random number  $K$  of “path clusters”, each cluster corresponding to a macro-level scattering path. Each path cluster is described by:

- A fraction of the total power;
- Central azimuth (horizontal) and elevation (vertical) angles of departure and arrival;
- Angular beamspreads around those central angles; and
- An absolute propagation time group delay of the cluster and power delay profile around the group delay.

In this work, we develop statistical models for the cluster power fractions and angular / spatial characteristics. However, we do not study temporal characteristics such as the relative propagation times or the time delay profiles. Due to the nature of the measurements, obtaining relative propagation times from different angular directions requires further analysis and will be subject of a forthcoming paper. The models here are only narrowband.

To fit the cluster model to our data, our first step was to detect the path clusters in the angular domain at each TX-RX location pair. As described above in Section II, at each location pair, the RX power was measured at various angular offsets. Since there are horizontal and vertical angles at both the transmitter and receiver, the measurements can be interpreted as a sampling of power measurements in a four-dimensional space.

A typical RX profile is shown in Fig. 3. Due to time, it was impossible to measure the entire four-dimensional angular space. Instead, at each location, only a subset of the angular offsets were measured. For example, in the location depicted in Fig. 3, the RX power was measured along two strips: one strip where the horizontal AoA was swept from 0 to 360 with the horizontal (azimuth) AoD varying in a 30 degree interval; and a second strip where the horizontal AoA was constant and the horizontal AoD was varied from 0 to 360. Two different values for the vertical (elevation) AoA were taken – the power measurements in each vertical AoA shown in three different subplots in Fig. 3. The vertical AoD was kept constant since there was less angular dispersion in that dimension. This measurement pattern was fairly typical, although in the 73 GHz measurements, we tended to measure more vertical AoA points.

The locations in white in Fig. 3 represent angular points where either the power was not measured, or the insufficient signal power was detected. Sufficient receive power to be validly was defined as finding at least a single path with 5dB SNR above the thermal noise. The power in all points that were either not measured or insufficient power was detected was treated as zero. If no valid angular points were detected, the location was considered in outage.

Detection of the spatial clusters amounts to finding regions in the four-dimensional angular space where the received energy is concentrated. This is a classic clustering problem, and for each candidate number of clusters  $K$ , we used a

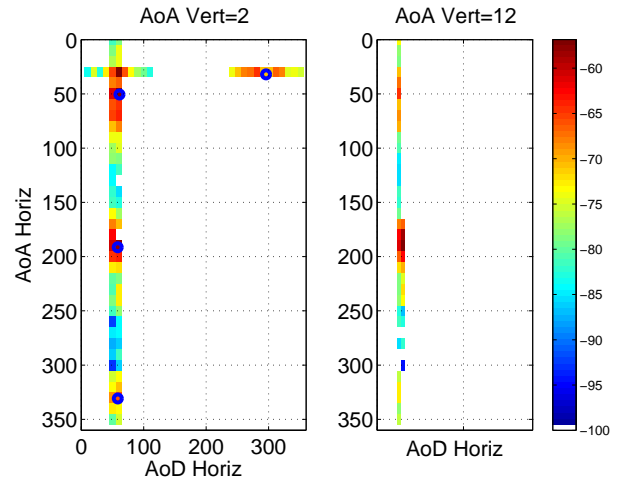


**Fig. 3:** Typical RX power angular profile at 28 GHz. Colors represent the average RX power in dBm at each angular offset, with white areas representing angular offsets that were either not measured, or had too low power to be validly detected. The blue circles represent the detected path cluster centers from our path clustering algorithm.

standard  $K$ -means clustering algorithm [45] to approximately find  $K$  clusters in the receive power domain with minimal angular dispersion. The  $K$ -means algorithm groups all the validly detected angular points into one of  $K$  clusters. For channel modeling in this paper, we use the algorithm to identify clusters with minimal angular variance as weighted by the receive power. The  $K$ -means algorithm performs this clustering by alternately (i) identifying the power weighted centroid of each cluster given a classification of the angular points into clusters; and (ii) updating the cluster identification by associating each angular point with its closest cluster center.

The clustering algorithm was run with increasing values of  $K$ , stopping when either of the following conditions were satisfied: (i) any two of the  $K$  detected clusters were within 2 standard deviations in all angular directions; or (ii) one of the clusters were empty. In this way, we obtain at each location, an estimate of the number of resolvable clusters  $K$ , their central angles, root-mean-squared angular spreads, and receive power. In the example location in Fig. 3, there were four detected clusters. The centers are shown in the left plot in the blue circles.

## C. Cluster Parameters

After detecting the clusters and the corresponding cluster parameters, we fit the following statistical models to the various cluster features.

a) *Number of clusters:* At the locations where a signal was detected (i.e. not in outage), the number of estimated clusters detected by our clustering algorithm, varied from 1 to 4. The measured distribution is plotted in the bar graph in Fig. 4 in the bars labeled “empirical”. Also, plotted is the distribution for a random variable  $K$  of the form,

$$K \sim \max\{Poisson(\lambda), 1\}, \quad (3)$$

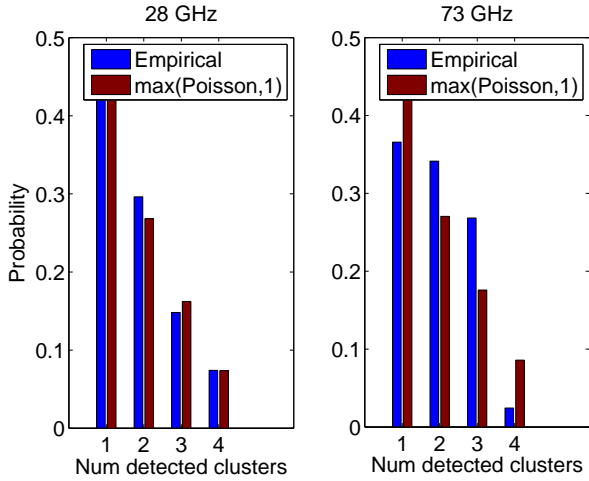


**Fig. 4:** Distribution of the number of detected clusters at 28 and 73 GHz. The measured distribution is labeled 'Empirical', which matches a Poisson distribution (3) well.

where  $\lambda$  set to empirical mean of  $K$ . It can be seen that this Poisson-max distribution is a good fit to the true number of detected clusters, particularly for 28 GHz.

*b) Cluster Power Fraction:* A critical component in the model is the distribution of power amongst the clusters. In the 3GPP model [25, Section B.1.2.2.1], the cluster power fractions are modeled as follows: T First, each cluster  $k$  has an absolute group delay,  $\tau_k$ , that is assumed to be exponentially distributed. Therefore, we can write  $\tau_k$  as

$$\tau_k = -r_\tau \sigma_\tau \log U_k \quad (4)$$

for a uniform random variable  $U_k \sim U[0, 1]$  and constants  $r_\tau$  and  $\sigma_\tau$ . The cluster  $k$  is assumed to have a power that scales by

$$\gamma'_k = \exp \left[ \tau_k \frac{r_\tau - 1}{\sigma_\tau r_\tau} \right] 10^{-0.1 Z_k}, \quad Z_k \sim \mathcal{N}(0, \zeta^2), \quad (5)$$

where the first term in the product places an exponential decay in the cluster power with the delay  $\tau_k$ , and the second term accounts for lognormal variations in the per cluster power with some variance  $\zeta^2$ . The final power fractions for the different clusters are then found by normalizing the values in (5) to unity, so that the fraction of power in  $k$ -th cluster is given by

$$\gamma_k = \frac{\gamma'_k}{\sum_{j=1}^K \gamma'_j}. \quad (6)$$

In the measurements in this study, we do not know the relative propagation delays  $\tau_k$  of the different clusters, so we treat them as unknown latent variables. Substituting (4) into (5), we obtain

$$\gamma'_k = U_k^{r_\tau - 1} 10^{-0.1 Z_k}, \quad U_k \sim U[0, 1], \quad Z_k \sim \mathcal{N}(0, \zeta^2), \quad (7)$$

The constants  $r_\tau$  and  $\zeta^2$  can then be treated as model parameters. Note that the lognormal variations  $Z_k$  in the per cluster power fractions (7) are distinct from the lognormal variations in total omnidirectional path loss (2).

For the mmW data, Fig. 5 shows the distribution of the fraction of power in the weaker cluster in the case when

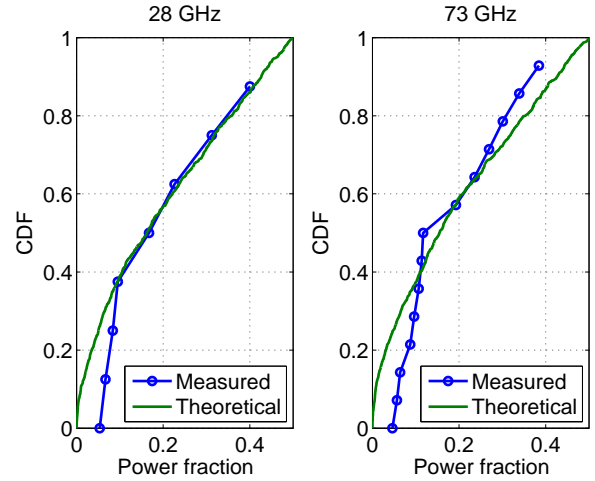


**Fig. 5:** Distribution of the fraction of power in the weaker cluster, when  $K = 2$  clusters were detected. Plotted are the measured distributions and the best fit of the theoretical model in (6) and (6).

$K = 2$  clusters were detected. Also plotted is the theoretical distribution based on (6) and (7) where the parameters  $r_\tau$  and  $\zeta^2$  were fit via an approximate maximum likelihood method. Since the measurement data we have does not have the relative delays of the different clusters we treat the variable  $U_k$  in (6) as an unknown latent variable, adding to the variation in the cluster power distributions. The estimated ML parameters are shown in Table I, with the values in 28 and 73 GHz being very similar.

We see that the 3GPP model with the ML parameter selection provides an excellent fit for the observed power fraction for clusters with more than 10% of the energy. The model is likely not fitting the very low energy clusters since our cluster detection is likely unable to find those clusters. However, for cases where the clusters have significant power, the model appears accurate. Also, since there were very few locations where the number of clusters was  $K \geq 3$ , we only fit the parameters based on the  $K = 2$  case. In the simulations below, we will assume the model is valid for all  $K$ .

*c) Angular Dispersion:* For each detected cluster, we measured the root mean-squared (rms) beamsread in the different angular dimensions. In the angular spread estimation in each cluster, we excluded power measurements from the lowest 10% of the total cluster power. This clipping introduces a small bias in the angular spread estimate. Although these low power points correspond to valid signals (as described above, all power measurements were only admitted into the data set if the signals were received with a minimum power level), the clipping reduced the sensitivity to misclassifications of points at the cluster boundaries. The distribution of the angular spreads at 28 GHz computed in this manner is shown in Fig. 6. Based on [46], we have also plotted an exponential distribution with the same empirical mean. We see that the exponential distribution provides a good fit of the data. Similar distributions were observed at 73 GHz, although they are not plotted here.

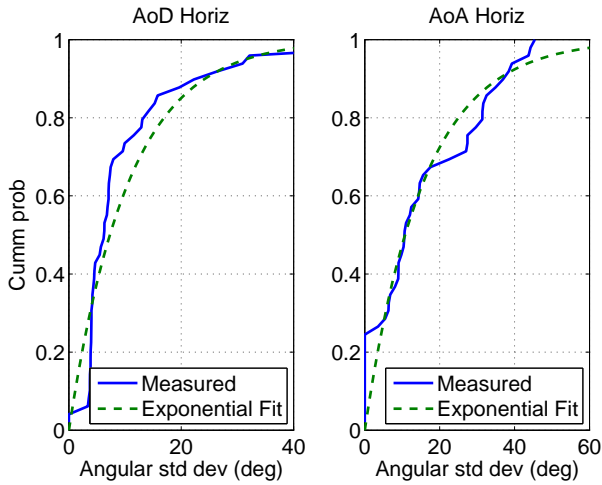


**Fig. 6:** Distribution of the rms angular spreads in the horizontal (azimuth) AoA and AoDs. Also plotted is an exponential distribution with the same empirical mean.

#### D. LOS, NLOS, and Outage Probabilities

Up to now, all the model parameters were based on locations not in outage. That is, there was some power detected in at least one delay in one angular location – See Section II. However, in many locations, particularly locations  $> 200\text{m}$  from the transmitter, it was simply impossible to detect any signal with transmit powers between 15 and 30 dBm. This outage is likely due to environmental obstructions that occlude all paths (either via reflections or scattering) to the receiver. The presence of outage in this manner is perhaps the most significant difference moving from conventional microwave / UHF to millimeter wave frequencies, and requires accurate modeling to properly assess system performance.

Current 3GPP evaluation methodologies such as [25] generally use a statistical model where each link is in either a LOS or NLOS state, with the probability of being in either state being some function of the distance. The path loss and other link characteristics are then a function of the link state, with potentially different models in the LOS and NLOS conditions. Outage occurs implicitly when the path loss in either the LOS or NLOS state is sufficiently large.

For mmW systems, we propose to add an additional state, so that each link can be in one of three conditions: LOS, NLOS or outage. In the outage condition, we assume there is no link between the TX and RX — that is, the path loss is infinite. By adding this third state with a random probability for a complete loss, the model provides a better reflection of outage possibilities inherent in mmW. As a statistical model, we assume probability functions for the three states are of the form:

$$p_{\text{out}}(d) = \max(0, 1 - e^{-a_{\text{out}}d + b_{\text{out}}}) \quad (8a)$$

$$p_{\text{LOS}}(d) = (1 - p_{\text{out}}(d))e^{-a_{\text{LOS}}d} \quad (8b)$$

$$p_{\text{NLOS}}(d) = 1 - p_{\text{out}}(d) - p_{\text{LOS}}(d) \quad (8c)$$

where the parameters  $a_{\text{LOS}}$ ,  $a_{\text{out}}$  and  $b_{\text{out}}$  are parameters that are fit from the data. The outage probability model (8a) is similar in form to the 3GPP suburban relay-UE NLOS model

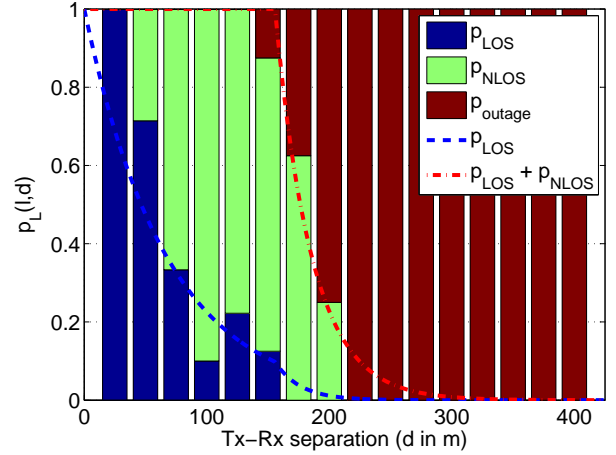


**Fig. 7:** The fitted curves and the empirical values of  $p_{\text{LOS}}(d)$ ,  $p_{\text{NLOS}}(d)$ , and  $p_{\text{out}}(d)$  as a function of the distance  $d$ . Measurement data is based on 42 TX-RX location pairs with distances from 30 m to 420 m at 28 GHz.

[25]. The form for the LOS probability (8b) can be derived on the basis of random shape theory [48]. See also [47] for a discussion on the outage modeling and its effect on capacity.

The parameters in the models were fit based on maximum likelihood estimation from the 42 TX-RX location pairs in the 28 GHz measurements in [24], [49]. In the simulations below, we assumed that the same probabilities held for the 73 GHz. The values are shown in Table I. Fig. 7 shows the fractions of points that were observed to be in each of the three states – outage, NLOS and LOS. Also plotted is the probability functions in (8) with the ML estimated parameter values. It can be seen that the probabilities provide an excellent fit.

That being said, caution should be exercised in generalizing these particular parameter values to other scenarios. Outage conditions are highly environmentally dependent, and further study is likely needed to find parameters that are valid across a range of circumstances. Nonetheless, we believe that the experiments illustrate that a three state model with an explicit outage state can provide a better description for variability in mmW link conditions. Below we will see assess the sensitivity of the model parameters to the link state assumptions.

#### E. Small-Scale Fading Simulation

The statistical models and parameters are summarized in Table I. These parameters all represent large-scale fading characteristics, meaning they are parameters associated with the macro-scattering environment and change relatively slowly [18].

One can generate a random narrowband time-varying channel gain matrix for these parameters following a similar procedure as the 3GPP / ITU model [25], [26] as follows: First, we generate random realizations of all the large-scale parameters in Table I including the distance-based omni path loss, the number of clusters  $K$ , their power fractions, central angles and angular beamspreads. For the small-scale fading model, each of the  $K$  path clusters can then be synthesized with a large number, say  $L = 20$ , of subpaths. Each subpath will

**TABLE I:** Proposed Statistical Model for the Large-scale Parameters based on the NYC data in [22].

Variable	Model	Model Parameter Values	
		28 GHz	73 GHz
Omnidirectional path loss, $PL$ and lognormal shadowing, $\xi$	$PL = \alpha + 10\beta \log_{10}(d) + \xi$ [dB] $\xi \sim \mathcal{N}(0, \sigma^2)$ , $d$ in meters	NLOS: $\alpha = 72.0, \beta = 2.92, \sigma = 8.7$ dB  LOS: $\alpha = 61.4, \beta = 2, \sigma = 5.8$ dB	NLOS: $\alpha = 86.6, \beta = 2.45, \sigma = 8.0$ dB (†) $\alpha = 82.7, \beta = 2.69, \sigma = 7.7$ dB (‡) LOS: $\alpha = 69.8, \beta = 2, \sigma = 5.8$ dB
NLOS-LOS-Outage probability	See (8)	$a_{\text{out}} = 0.0334\text{m}^{-1}, b_{\text{out}} = 5.2, a_{\text{los}} = 0.0149\text{m}^{-1}$	
Number of clusters, $K$	$K \sim \max\{\text{Poisson}(\lambda), 1\}$	$\lambda = 1.8$	$\lambda = 1.9$
Cluster power fraction	See (6) and (7): $\gamma'_k = U_k^{r_\tau - 1} 10^{0.1 Z_k}$ , $Z_k \sim \mathcal{N}(0, \zeta^2), U_k \sim U[0, 1]$	$r_\tau = 2.8, \zeta = 4.0$	$r_\tau = 3.0, \zeta = 4.0$
BS and UE horizontal cluster central angles, $\theta$	$\theta \sim U(0, 2\pi)$		
BS and UE vertical cluster central angles, $\phi$	$\phi = \text{LOS elevation angle}$		
BS cluster rms angular spread	$\sigma$ is exponentially distributed, $\mathbb{E}(\sigma) = \lambda^{-1}$	Horiz $\lambda^{-1} = 10.2^\circ$ ; Vert $\lambda^{-1} = 0^\circ$ (*)	Horiz $\lambda^{-1} = 10.5^\circ$ ; Vert $\lambda^{-1} = 0^\circ$ (*)
UE rms angular spread	$\sigma$ is exponentially distributed, $\mathbb{E}(\sigma) = \lambda^{-1}$	Horiz $\lambda^{-1} = 15.5^\circ$ ; Vert $\lambda^{-1} = 6.0^\circ$	Horiz $\lambda^{-1} = 15.4^\circ$ ; Vert $\lambda^{-1} = 3.5^\circ$

Note: The model parameters are derived in based on converting the directional measurements from the NYC data in [22], and assuming an isotropic (omnidirectional, unity gain) channel model with the 49 dB of antenna gains removed from the measurements.

(†) Parameters for the 2m-RX-height data and 4.06m-RX-height data combined.

(‡) Parameters for the 2m-RX-height data only.

(\*) BS downtilt was fixed at 10 degree for all measurements, resulting in no measurable vertical angular spread at BS.

have horizontal and vertical AoAs,  $\theta_{k\ell}^{rx}, \phi_{k\ell}^{rx}$ , and horizontal and vertical AoDs,  $\theta_{k\ell}^{tx}, \phi_{k\ell}^{tx}$ , where  $k = 1, \dots, K$  is the cluster index and  $\ell = 1, \dots, L$  is the subpath index within the cluster. These angles can be generated as wrapped Gaussians around the cluster central angles with standard deviation given by the rms angular spreads for the cluster. Then, if there are  $n_{rx}$  RX antennas and  $n_{tx}$  TX antennas, the narrowband time-varying channel gain between a TX-RX pair can be represented by a matrix (see, for example, [50] for more details):

$$\mathbf{H}(t) = \frac{1}{\sqrt{L}} \sum_{k=1}^K \sum_{\ell=1}^L g_{k\ell}(t) \mathbf{u}_{rx}(\theta_{k\ell}^{rx}, \phi_{k\ell}^{rx}) \mathbf{u}_{tx}^*(\theta_{k\ell}^{tx}, \phi_{k\ell}^{tx}), \quad (9)$$

where  $g_{k\ell}(t)$  is the complex small-scale fading gain on the  $\ell$ -th subpath of the  $k$ -th cluster and  $\mathbf{u}_{rx}(\cdot) \in \mathbb{C}^{n_{rx}}$  and  $\mathbf{u}_{tx}(\cdot) \in \mathbb{C}^{n_{tx}}$  are the vector response functions for the RX and TX antenna arrays to the angular arrivals and departures. The small-scale coefficients would be given by

$$g_{k\ell}(t) = \bar{g}_{k\ell} e^{2\pi i t f_{dmax} \cos(\omega_{k\ell})}, \quad \bar{g}_{k\ell} \sim \mathcal{CN}(0, \gamma_k 10^{-0.1 PL}),$$

where  $f_{dmax}$  is the maximum Doppler shift,  $\omega_{k\ell}$  is the angle of arrival of the subpath relative to the direction of motion and  $PL$  is the omnidirectional path loss. The relation between  $\omega_{k\ell}$  and the angular arrivals  $\theta_{k\ell}^{rx}$  and  $\phi_{k\ell}^{rx}$  will depend on the orientation of the mobile RX array relative to the motion. Note that the model (9) is only a narrowband model since we have not yet characterized the delay spread.

#### IV. COMPARISON TO 3GPP CELLULAR MODELS

##### A. Path Loss Comparison

It is useful to briefly compare the distance-based path loss we observed for mmW signals with models for conventional

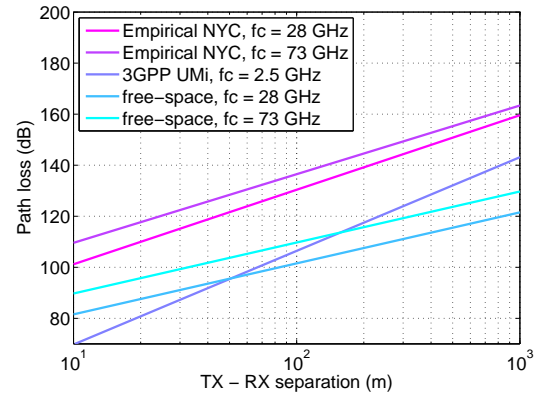


**Fig. 8:** Comparison of distance-based path loss models. The curves labeled “Empirical NYC” are the mmW models derived in this paper for 28 and 73 GHz. These are compared to free-space propagation for the same frequencies and 3GPP Urban Micro (UMi) model for 2.5 GHz.

cellular systems. To this end, Fig. 8 plots the median effective total path loss as a function of distance for several different models:

- *Empirical NYC:* These curves are the omnidirectional path loss predicted by our linear model (2). Plotted is the median path loss

$$PL(d) \text{ [dB]} = \alpha + 10\beta \log_{10}(d), \quad (10)$$

where  $d$  is the distance and the  $\alpha$  and  $\beta$  parameters are the NLOS values in Table I. For 73 GHz, we have plotted the 2.0 UE height values.

- *Free space*: The theoretical free space path loss is given by Friis' Law [18]. We see that, at  $d = 100$  m, the free space path loss is approximately 30 dB less than the model we have experimentally measured here. Thus, many of the works such as [7], [35] that assume free-space propagation may be somewhat optimistic in their capacity predictions. Also, it is interesting to point out that one of the models assumed in the Samsung study [4] (PLF1) is precisely free space propagation + 20 dB – a correction factor that is also somewhat more optimistic than our experimental findings.
- *3GPP UMi*: The standard 3GPP urban micro (UMi) path loss model with hexagonal deployments [25] is given by

$$PL(d) \text{ [dB]} = 22.7 + 36.7 \log_{10}(d) + 26 \log_{10}(f_c), \quad (11)$$

where  $d$  is distance in meters and  $f_c$  is the carrier frequency in GHz. Fig. 8 plots this path loss model at  $f_c = 2.5$  GHz. We see that our propagation models at both 28 and 73 GHz predict omnidirectional path losses that, for most of the distances, are approximately 20 to 25 dB higher than the 3GPP UMi model at 2.5 GHz. However, since the wavelengths at 28 and 73 GHz are approximately 10 to 30 times smaller, this path loss can be entirely compensated with sufficient beamforming on either the transmitter or receiver with the same physical antenna size. Moreover, if beamforming is applied on both ends, the effective path loss can be even lower in the mmW range. We conclude that, barring outage events and maintaining the same physical antenna size, *mmW signals do not imply any reduction in path loss relative to current cellular frequencies, and in fact, be improved over today's systems.*

### B. Spatial Characteristics

We next compare the spatial characteristics of the mmW and microwave models. To this end, we can compare the experimentally derived mmW parameters in Table I with those, for example, in [25, Table B.1.2.2.1-4] for the 3GPP urban microcell model – the layout that would be closest to our deployment. We immediately see that the angular spread of the clusters are similar in the mmW and 3GPP UMi models. While the 3GPP UMi model has somewhat more clusters, it is possible that multiple distinct clusters were present in the mmW scenario, but were not visible since we did not perform any temporal analysis of the data. That is, in our clustering algorithm above, we group power from different time delays together in each angular offset.

Another interesting comparison is the delay scaling parameter,  $r_\tau$ , which governs how relative propagation delays between clusters affects their power fraction. Table I shows values of  $r_\tau$  of 2.8 and 3.0, which are in the same range as the values in the 3GPP UMi model [25, Table B.1.2.2.1-4] suggesting that the power delay may be similar. This property would, however, require further confirmation with actual relative propagation delays between clusters.

### C. Outage Probability

One final difference that should be noted is the outage probability. In the standard 3GPP models, the event that a channel is completed obstructed is not explicitly modeled. Instead, channel variations are accounted for by lognormal shadowing along with, in certain models, wall and other obstruction losses. However, we see in our experimental measurements that channels in the mmW range can experience much more significant blockages that are not well-modeled via these more gradual terms. We will quantify the effects of the outages on the system capacity below.

## V. CHANNEL SPATIAL CHARACTERISTICS AND MIMO GAINS

A significant gain for mmW systems derives from the capability of high-dimensional beamforming. Current technology can easily support antenna arrays with 32 elements and higher [6], [10]–[17]. Although our simulations below will assess the precise beamforming gains in a micro-cellular type deployment, it is useful to first consider some simple spatial statistics of the channel to qualitatively understand how large the beamforming gains may be and how they can be practically achieved.

### A. Beamforming in Millimeter Wave Frequencies

However, before examining the channel statistics, we need to point out two unique aspects of beamforming and spatial multiplexing in the mmW range. First, a full digital front-end with high resolution A/D converters on each antenna across the wide bandwidths of mmW systems may be prohibitive in terms of cost and power, particularly for mobile devices [4]–[6], [51]. Most commercial designs have thus assumed phased-array architectures where signals are combined either in RF with phase shifters [52]–[54] or at IF [55]–[57] prior to the A/D conversion. While greatly reducing the front-end power consumption, this architecture may limit the number of separate spatial streams that can be processed since each spatial stream will require a separate phased-array and associated RF chain. Such limitations will be particularly important at the UE.

A second issue is the channel coherence: due to the high Doppler frequency it may not be feasible to maintain the channel state information (CSI) at the transmitter, even in TDD. In addition, full CSI at the receiver may also not be available since the beamforming must be applied in analog and hence the beam may need to be selected without separate digital measurements on the channels on different antennas.

### B. Instantaneous vs. Long-Term Beamforming

Under the above constraints, we begin by trying to assessing what the rough gains we can expect from beamforming are as follows: Suppose that the transmitter and receiver apply complex beamforming vectors  $\mathbf{v}_{tx} \in \mathbb{C}^{n_{tx}}$  and  $\mathbf{v}_{rx} \in \mathbb{C}^{n_{rx}}$  respectively. We will assume these vectors are normalized to unity:  $\|\mathbf{v}_{tx}\| = \|\mathbf{v}_{rx}\| = 1$ . Apply these beamforming vectors



will reduce the MIMO channel  $\mathbf{H}$  in (9) to an effective SISO channel with gain given by

$$G(\mathbf{v}_{tx}, \mathbf{v}_{rx}, \mathbf{H}) = |\mathbf{v}_{rx}^* \mathbf{H} \mathbf{v}_{tx}|^2.$$

The maximum value for this gain would be

$$G_{\text{inst}}(\mathbf{H}) = \max_{\|\mathbf{v}_{tx}\|=\|\mathbf{v}_{rx}\|=1} G(\mathbf{v}_{tx}, \mathbf{v}_{rx}, \mathbf{H}),$$

and is found from the left and right singular vectors of  $\mathbf{H}$ . We can evaluate the average value of this gain as a ratio:

$$\text{BFGain}_{\text{inst}} := 10 \log_{10} \left[ \frac{\mathbb{E} G_{\text{inst}}(\mathbf{H})}{G_{\text{omni}}} \right], \quad (12)$$

where we have compared the gain with beamforming to the omnidirectional gain

$$G_{\text{omni}} := \frac{1}{n_{rx} n_{tx}} \mathbb{E} \|\mathbf{H}\|_F^2, \quad (13)$$

and the expectations in (12) and (13) be taken over the small scale fading parameters in (9), holding the large-scale fading parameters constant. The ratio (12) represents the maximum increase in the gain (effective decrease in path loss) from optimally steering the TX and RX beamforming vectors. It is easily verified that this gain is bounded by

$$\text{BFGain}_{\text{inst}} \leq 10 \log_{10}(n_{rx} n_{tx}), \quad (14)$$

with equality when  $\mathbf{H}$  in (9) is rank one – that is, there is no angular dispersion and the energy is concentrated in a single direction. In mmW systems, if the gain bound (14) can be achieved, the gain would be large: for example, if  $n_{tx} = 64$  and  $n_{rx} = 16$ , the maximum gain in (14) is  $10 \log_{10}((64)(16)) \approx 30$  dB. We call the gain in (12) the *instantaneous gain* since it represents the gain when the TX and RX beamforming vectors can be selected based on the instantaneous small-scale fading realization of the channel, and thus requires CSI at both the TX and RX. As described above, such instantaneous beamforming may not be feasible.

We therefore consider an alternative and more conservative approach known as *long-term* beamforming as described in [58]. In long-term beamforming, the TX and RX adapt the beamforming vectors to the large-scale parameters (which are relatively slowly varying) but not the small-scale ones. One approach is to simply align the TX and RX beamforming directions to the maximal eigenvectors of the covariance matrices,

$$\mathbf{Q}_{rx} := \mathbb{E}[\mathbf{H}\mathbf{H}^*], \quad \mathbf{Q}_{tx} := \mathbb{E}[\mathbf{H}^*\mathbf{H}], \quad (15)$$

where the expectations are taken with respect to the small-scale fading parameters assuming the large-scale parameters are constant. Since the small-scale fading is averaged out, these covariance matrices are coherent over much longer periods of time and can be estimated much more accurately.

When the beamforming vectors are held constant over the small-scale fading, we obtain a SISO Rayleigh fading channel with an average gain of  $\mathbb{E}G(\mathbf{v}_{tx}, \mathbf{v}_{rx}, \mathbf{H})$ , where the expectation is again taken over the small-scale fading. We can define the *long-term beamforming gain* as the ratio

between the average gain with beamforming and the average omnidirectional gain in (13),

$$\text{BFGain}_{\text{long}} = 10 \log_{10} \left[ \frac{\mathbb{E}G(\mathbf{v}_{tx}, \mathbf{v}_{rx}, \mathbf{H})}{G_{\text{omni}}} \right], \quad (16)$$

where the beamforming vectors  $\mathbf{v}_{tx}$  and  $\mathbf{v}_{rx}$  are selected from the maximal eigenvectors of the covariance matrices  $\mathbf{Q}_{rx}$  and  $\mathbf{Q}_{tx}$ .

The long-term beamforming gain (16) will be less than the instantaneous gain (12). To simplify the calculations, we can approximately evaluate the long-term beamforming gain (16), assuming a well-known Kronecker model [59], [60],

$$\mathbf{H} \approx \frac{1}{\sqrt{\text{Tr}(\mathbf{Q}_{rx})}} \mathbf{Q}_{rx}^{1/2} \mathbf{P} \mathbf{Q}_{tx}^{1/2}, \quad (17)$$

where  $\mathbf{P}$  is an i.i.d. matrix with complex Gaussian zero mean, unit variance components. Under this approximate model, it is easy to verify that the gain (16) is given by the sum

$$\text{BFGain}_{\text{long}} \approx \text{BFGain}_{TX} + \text{BFGain}_{RX}, \quad (18)$$

where the RX and TX beamforming gains are given by

$$\text{BFGain}_{RX} = 10 \log_{10} \left[ \frac{\lambda_{\max}(\mathbf{Q}_{rx})}{(1/n_{rx}) \sum_i \lambda_i(\mathbf{Q}_{rx})} \right] \quad (19a)$$

$$\text{BFGain}_{TX} = 10 \log_{10} \left[ \frac{\lambda_{\max}(\mathbf{Q}_{tx})}{(1/n_{tx}) \sum_i \lambda_i(\mathbf{Q}_{tx})} \right], \quad (19b)$$

where  $\lambda_i(\mathbf{Q})$  is the  $i$ -th eigenvalue of  $\mathbf{Q}$  and  $\lambda_{\max}(\mathbf{Q})$  is the maximal eigenvalue.

Fig. 9 plots the distributions of the long-term beamforming gains for the UE and BS using the experimentally-derived channel model for 28 GHz along with (19) (Note that  $\text{BFGain}_{RX}$  and  $\text{BFGain}_{TX}$  can be used for either the BS or UE – the gains are the same in either direction). In this figure, we have assumed a half-wavelength 8x8 uniform planar array at the BS transmitter and 4x4 uniform planar array at the UE receiver. The beamforming gains are random quantities since they depend on the large-scale channel parameters. The distribution of the beamforming gains at the TX and RX along the serving links are shown in Fig. 9 in the curves labeled “Serving links”. Since we have assumed  $n_{rx} = 4^2 = 16$  antennas and  $n_{tx} = 8^2 = 64$  antennas, the maximum beamforming gains possible would be 12 and 18 dB respectively, and we see that long-term beamforming is typically able to get within 2-3 dB of this maximum. The average gain for instantaneous beamforming will be somewhere between the long-term beamforming curve and the maximum value, so we conclude that loss from long-term beamforming with respect to instantaneous beamforming is typically bounded by 2-3 dB at most.

Also plotted in Fig. 9 is the distribution of the typical gain along an interfering link. This interfering gain provides a measure of how directionally isolated a typical interferer will be. The gain is estimated by selecting the beamforming direction from a typical second-order matrix  $\mathbf{Q}_{rx}$  or  $\mathbf{Q}_{tx}$  and then applying that beamforming direction onto a random second-order gain with the same elevation angles. The same elevation angles are used since the BSs will likely have the same height. We see that the beamforming gains along

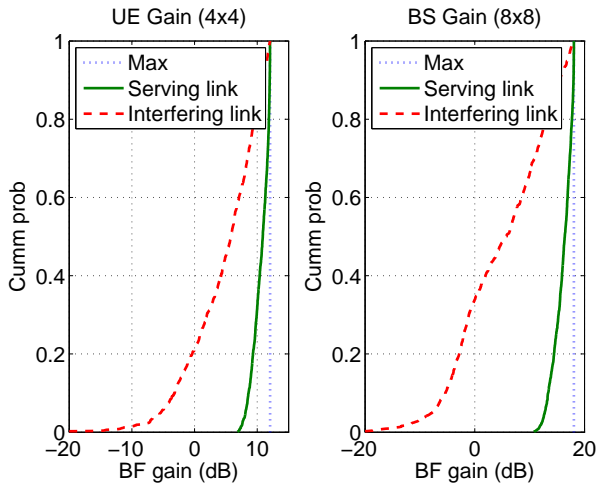


**Fig. 9:** Distributions of the BS and UE long-term beamforming gains based on the 28 GHz models. The

these interfering directions is significantly lower. The median interfering beamforming gain is approximately 6 dB lower in the RX and 9 dB in the TX. This difference in gains suggests that beamforming in mmW systems will be very effective in achieving a high level of directional isolation.

Although the plots were shown for 28 GHz, very similar curves were observed at 73 GHz.

### C. Spatial Degrees of Freedom

A second useful statistic to analyze is the typical rank of the channel. The fact that we observed multiple path clusters between each TX-RX location pair indicates the possibility of gains from spatial multiplexing [50]. To assess the amount of energy in multiple spatial streams, define

$$\phi(r) := \frac{1}{\mathbb{E}\|\mathbf{H}\|_F^2} \max_{\mathbf{V}_{rx}, \mathbf{V}_{tx}} \mathbb{E}\|\mathbf{V}_{rx}^* \mathbf{H} \mathbf{V}_{tx}\|_F^2,$$

where the maximum is over matrices  $\mathbf{V}_{rx} \in \mathbb{C}^{n_{rx} \times r}$  and  $\mathbf{V}_{tx} \in \mathbb{C}^{n_{tx} \times r}$  with  $\mathbf{V}_{rx}^* \mathbf{V}_{rx} = \mathbf{I}_r$  and  $\mathbf{V}_{tx}^* \mathbf{V}_{tx} = \mathbf{I}_r$ . The quantity  $\phi(r)$  represents the fraction of energy that can be captured by precoding onto an optimal  $r$ -dimensional subspace at both the RX and TX. Under the Kronecker model approximation (17), a simple calculation shows that this power fraction is given by the  $r$  largest eigenvalues,

$$\phi(r) = \left[ \frac{\sum_{i=1}^r \lambda_i(\mathbf{Q}_{rx})}{\sum_{i=1}^{n_{rx}} \lambda_i(\mathbf{Q}_{rx})} \right] \left[ \frac{\sum_{i=1}^r \lambda_i(\mathbf{Q}_{tx})}{\sum_{i=1}^{n_{tx}} \lambda_i(\mathbf{Q}_{tx})} \right],$$

where  $\mathbf{Q}_{rx}$  and  $\mathbf{Q}_{tx}$  are the spatial covariance matrices (15) and  $\lambda_i(\mathbf{Q})$  is the  $i$ -th largest eigenvalue of  $\mathbf{Q}$ . Since the power fraction is dependent on the second-order, long-term channel statistics, it is a random variable. Fig. 10 plots the distribution of  $\phi(r)$  for values  $r = 1, \dots, 4$  for the experimentally-derived 28 GHz channel model. The power fractions for the 73 GHz are not plotted, but are similar.

If the channel had no angular dispersion per cluster, then  $\mathbf{Q}_{rx}$  and  $\mathbf{Q}_{tx}$  would have rank one and all the energy could be captured with one spatial dimension, i.e.  $\phi(r) = 1$  with  $r = 1$ . However, since the channels have possibly multiple clusters and the clusters have a non-zero angular dispersion, we see

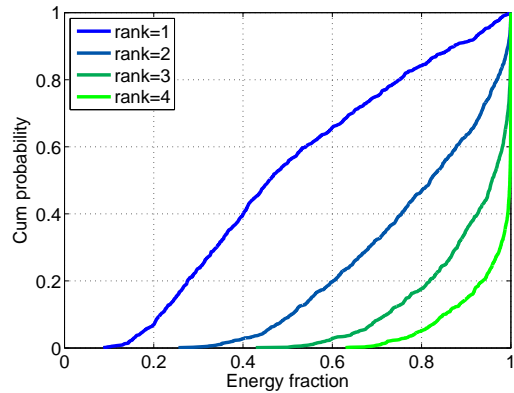


**Fig. 10:** Distribution of the energy fraction in  $r$  spatial directions for the 28 GHz channel model.

**TABLE II:** Default network parameters

Parameter	Description
BS layout and sectorization	Hexagonally arranged cell sites placed in a 2km x 2km square area with three cells per site.
UE layout	Uniformly dropped in area with average of 10 UEs per BS cell (i.e. 30 UEs per cell site).
Inter-site distance (ISD)	200 m
Carrier frequency	28 and 73 GHz
Duplex mode	TDD
Transmit power	20 dBm (uplink), 30 dBm (downlink)
Noise figure	5 dB (BS), 7 dB (UE)
BS antenna	8x8 $\lambda/2$ uniform planar array
UE antenna	4x4 $\lambda/2$ uniform planar array for 28 GHz and 8x8 array for 73 GHz.
Beamforming	Long-term, single stream

that there is significant energy in higher spatial dimensions. For example, Fig. 10 shows that in the median channel, a single spatial dimension is only able to capture approximately 50% of the channel energy. Two degrees of freedom are needed to capture the 80% of the channel energy and three dimensions are needed for 95%. These numbers suggest that many locations will be capable of providing single-user MIMO gains with two and even three streams. Note that further spatial degrees of freedom are possible with multi-user MIMO beyond the rank of the channel to any one user.

## VI. CAPACITY EVALUATION

### A. System Model

To assess the system capacity under the experimentally-measured channel models, we follow a standard cellular evaluation methodology [25] where the BSs and UEs are randomly “dropped” according to some statistical model and the performance metrics are then measured over a number of random realizations of the network. Since we are interested in small cell networks, we follow a BS and UE distribution similar to the 3GPP Urban Micro (UMi) model in [25] with some parameters taken from the Samsung mmW study [4],

[5]. The specific parameters are shown in Table II. Similar to 3GPP UMi model, the BS cell sites are distributed in a uniform hexagonal pattern with three cells (sectors) per site covering a 2 km by 2 km area with an inter-site distance (ISD) of 200 m. This layout leads to 130 cell sites (390 cells) per drop. UEs are uniformly distributed over the area at a density of 10 UEs per cell – which also matches the 3GPP UMi assumptions. The maximum transmit power of 20 dBm at the UE and 30 dBm are taken from [4], [5]. Note that since our channel models were based on data from receivers in outdoor locations, implicit in our model is that all users are outdoors. If we included mobiles that were indoor, it is likely that the capacity numbers would be significantly lower since mmW signals cannot penetrate many building materials.

These transmit powers are reasonable since current CMOS RF power amplifiers in the mmW range exhibit peak efficiencies of at least 8% [61], [62]. This implies that the UE TX power of 20 dBm and BS TX power of 30 dBm can be achieved with powers of 1.25W and 12.5W, respectively.

### B. Beamforming Modeling

Although our preliminary calculations in Section V-C suggest that the channel may support spatial multiplexing, we consider only single stream processing where the RX and TX beamforming is designed to maximize SNR without regard to interference. That is, there is no interference nulling. It is possible that more advanced techniques such as inter-cell coordinated beamforming and MIMO spatial multiplexing [35], [51] may offer further gains, particularly for mobiles close to the cell. Indeed, as we saw in Section V-C, many UEs have at least two significant spatial degrees of freedom to support single user MIMO. Multiuser MIMO and SDMA may offer even greater opportunities for spatial multiplexing. However, modeling of MIMO and SDMA, particularly under constraints on the number of spatial streams requires further work and will be studied in upcoming papers.

Under the assumption of signal stream processing, the link between each TX-RX pair can be modeled as an effective single-input single-output (SISO) channel with an effective path loss that accounts for the total power received on the different path clusters between the TX and RX and the beamforming applied at both ends of the link. The beamforming gain will be distributed following the distributions in Section V-B.

### C. MAC Layer Assumptions

Once the effective path losses are determined between all TX-RX pairs, we can compute the average SINR at each RX. The SINR in turn determines the rate per unit time and bandwidth allocated to the mobile. In an actual cellular system, the achieved rate (goodput) will depend on the average SNR through a number of factors including the channel code performance, channel quality indicator (CQI) reporting, rate adaptation and Hybrid automatic repeat request (HARQ) protocol. In this work, we abstract this process and assume a simplified, but widely-used, model [63], where the spectral

efficiency is assumed to be given by the Shannon capacity with some loss  $\Delta$ :

$$\rho = \min \left\{ \log_2 \left( 1 + 10^{0.1(\text{SNR}-\Delta)} \right), \rho_{max} \right\}, \quad (20)$$

where  $\rho$  is the spectral efficiency in bps/Hz, the SNR and loss factor  $\Delta$  are in dB, and  $\rho_{max}$  is the maximum spectral efficiency. Based on analysis of current LTE turbo codes, the paper [63] suggests parameters  $\Delta = 1.6$  dB and  $\rho_{max} = 4.8$  bps/Hz. Assuming similar codes can be used for a mmW system, we apply the same  $\rho_{max}$  in this simulation, but increase  $\Delta$  to 3 dB to account for fading. This increase in  $\Delta$  is necessary since the results in [63] are based on AWGN channels. The 1.4 dB increase used here is consistent with results from link error prediction methods such as [64]. Note that all rates stated in this paper *do not* include the half duplex loss, which must be added depending on the UL-DL ratio. The one exception to this accounting is the comparison in Section VI-D between mmW and LTE systems, where we explicitly assume a 50-50 UL-DL duty cycle.

For the uplink and downlink scheduling, we use proportional fair scheduling with full buffer traffic. Since we assume that we cannot exploit multi-user diversity and only schedule on the average channel conditions, the proportional fair assumption implies that each UE will get an equal fraction of the time-frequency resources. In the uplink, we will additionally assume that the multiple access scheme enables multiple UEs to be scheduled at the same time. In OFDMA systems such as LTE, this can be enabled by scheduled the UEs on different resource blocks. Enabling multiple UEs to transmit at the same time provides a significant power boost. However, supporting such multiple access also requires that the BS can receive multiple simultaneous beams. As mentioned above, such reception would require multiple RF chains at the BS, which will add some complexity and power consumption. Note, however, that all processing in this study, requires only single streams at the mobile, which is the node that is more constrained in terms of processing power.

### D. Uplink and Downlink Throughput

We plot SINR and rate distributions in Figs. 11 and 12 respectively. The distributions are plotted for both 28 and 73 GHz and for 4x4 and 8x8 arrays at the UE. The BS antenna array is held at 8x8 for all cases. There are a few important observations we can make.

First, for the same number of antenna elements, the rates for 73 GHz are approximately half the rates for the 28 GHz. However, a 4x4  $\lambda/2$ -array at 28 GHz would take about the same area as an 8x8  $\lambda/2$  array at 73 GHz. Both would be roughly  $1.5 \times 1.5$  cm<sup>2</sup>, which could be easily accommodated in a handheld mobile device. In addition, we see that 73 GHz 8x8 rate and SNR distributions are very close to the 28 GHz 4x4 distributions, which is reasonable since we are keeping the antenna size constant. Thus, we can conclude that the loss from going to the higher frequencies can be made up from larger numbers of antenna elements without increasing the physical antenna area.

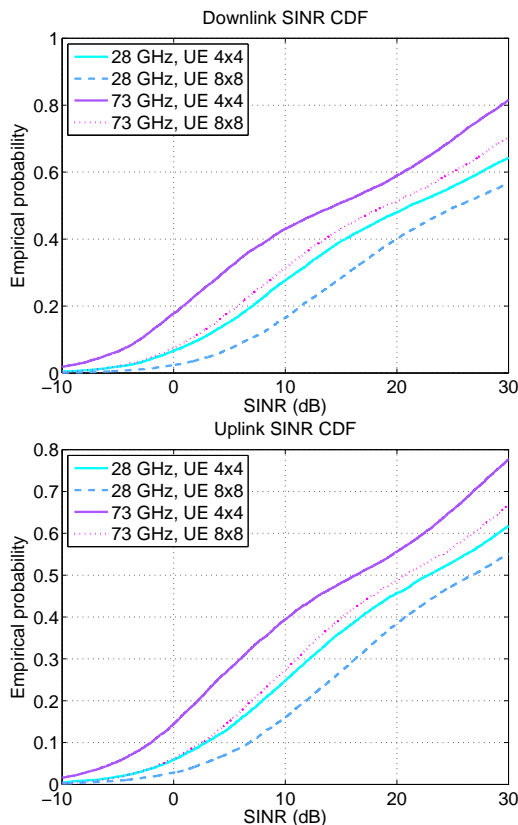


**Fig. 11:** Downlink (top plot) / uplink (bottom plot) SINR CDF at 28 and 73 GHz with 4x4 and 8x8 antenna arrays at the UE. The BS antenna array is held at 8x8.

As a second point, we can compare the SINR distributions in Fig. 11 to those of a traditional cellular network. Although the SINR distribution for a cellular network in a traditional frequency is not plotted here, the SINR distributions in Fig. 11 are actually slightly better than those found in cellular evaluation studies [25]. For example, in Fig. 11, only about 5 to 10% of the mobiles appear under 0 dB, which is a lower fraction than typical cellular deployments. We conclude that, although mmW systems have an omnidirectional path loss that is 20 to 25 dB worse than conventional microwave frequencies, short cell radii combined with highly directional beams are able to completely compensate for the loss.

As one final point, Table III provides a comparison of mmW and current LTE systems. The LTE capacity numbers are taken from the average of industry reported evaluations given in [25] – specifically Table 10.1.1.1-1 for the downlink and Table 1.1.1.3-1 for the uplink. The LTE evaluations include advanced techniques such as SDMA, although not coordinated multipoint. For the mmW capacity, we assumed 50-50 UL-DL TDD split and a 20% control overhead in both the UL and DL directions. Note that in the spectral efficiency numbers for the mmW system, we have included the 20% overhead, but not the 50% UL-DL split. Hence the cell throughput is given by  $C = 0.5\rho W$ , where  $\rho$  is the spectral efficiency,  $W$  is the bandwidth, and the 0.5 accounts for the duplexing.

Under these assumptions, we see that the mmW system for either the 28 GHz 4x4 array or 73 GHz 8x8 array provides

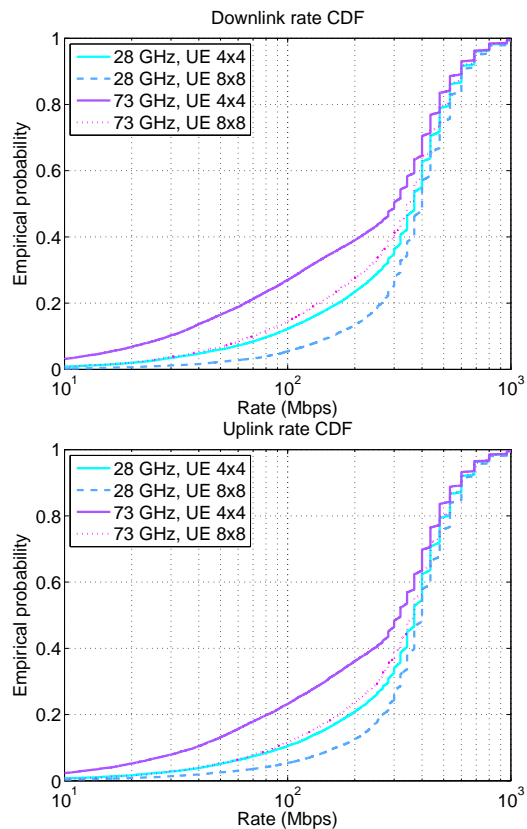


**Fig. 12:** Downlink (top plot) / uplink (bottom plot) rate CDF at 28 and 73 GHz with 4x4 and 8x8 antenna arrays at the UE. The BS antenna array is held at 8x8.

a significant  $> 25$ -fold increase of overall cell throughput over the LTE system. Of course, most of the gains are simply coming from the increased spectrum: the operating bandwidth of mmW is chosen as 1 GHz as opposed to 20+20 MHz in LTE – so the mmW system has 25 times more bandwidth. However, this is a basic mmW system with no spatial multiplexing or other advanced techniques – we expect even higher gains when advanced technologies are applied to optimize the mmW system. While the lowest 5% cell edge rates are less dramatic, they still offer a 10 to 13 fold increase over the LTE cell edge rates.

### E. Directional Isolation

In addition to the links being in a relatively high SINR, an interesting feature of mmW systems is that thermal noise dominates interference. Although the distribution of the interference to noise ratio is not plotted, we observed that in 90% of the links, thermal noise was larger than the interference – often dramatically so. We conclude that highly directional transmissions used in mmW systems combined with short cell radii result in links that are in relatively high SINR with little interference. This feature is in stark contrast to current dense cellular deployments where links are overwhelmingly interference-dominated.

**TABLE III:** mmW and LTE cell throughput/cell edge rate comparison.

System	System Bandwidth	UE ant	NLOS-LOS-Outage model	Spec. eff (bps/Hz)		Cell throughput (Mbps/cell)		5% Cell edge rate (Mbps/UE)	
				DL	UL	DL	UL	DL	UL
28 GHz mmW	1 GHz TDD	8x8	Hybrid	3.34	3.16	1668	1580	52.28	34.78
		4x4	Hybrid	3.03	2.94	1514	1468	28.47	19.90
			Hybrid, $d_{\text{shift}} = 50\text{m}$	2.90	2.91	1450	1454	17.62	17.49
			Hybrid, $d_{\text{shift}} = 75\text{m}$	2.58	2.60	1289	1298	0.54	0.09
			No LOS, $d_{\text{shift}} = 50\text{m}$	2.16	2.34	1081	1168	11.14	15.19
73 GHz mmW	1 GHz TDD	4x4	Hybrid	2.58	2.58	1288	1291	10.02	8.92
		8x8	Hybrid	2.93	2.88	1465	1439	24.08	19.76
2.5 GHz LTE	20+20 MHz FDD	2		2.69	2.36	53.8	47.2	1.80	1.94

Note 1. Assumes 20% overhead, 50% UL-DL duty cycle and 8x8 BS antennas for the mmW system

Note 2. Assumes 2 TX 4 RX antennas at BS side for LTE system

Note 3. Long-term, non-coherent beamforming are assumed at both the BS and UE in the mmW system. However, the mmW results assume no spatial multiplexing gains, whereas the LTE results from [25] include spatial multiplexing and beamforming.

### F. Effect of Outage

One of the significant features of mmW systems is the presence of outage – the fact that there is a non-zero probability that the signal from a given BS can be completely blocked and hence not detectable. The parameters in the hybrid LOS-NLOS-outage model (8) were based on our data in one region of NYC. To understand the potential effects of different outage conditions, Fig. 13 shows the distribution of rates under various NLOS-LOS-outage probability models. The curve labeled “hybrid,  $d_{\text{shift}} = 0$ ” is the baseline model with parameters provided on Table I that we have used up to now. These are the parameters based on the fitting the NYC data. This model is compared to two models with heavier outage created by shifting  $p_{\text{out}}(d)$  to the left by 50 m and 75 m, shown in the second and third curves. The fourth curve labeled “NLOS+outage,  $d_{\text{shift}} = 50\text{m}$ ” uses the shifted outage and also removes all the LOS links – hence all the links are either in an outage or NLOS state. In all cases, the carrier frequency is 28 GHz and the we assumed a 4x4 antenna array at the UE. Similar findings were observed at 73 GHz and 8x8 arrays.

We see that, even with a 50 m shift in the outage curve (i.e. making the outages occur 50 m closer than predicted by our model), the system performance is not significantly affected. In fact, there is a slight improvement in UL rates due to suppressed interference and only slight decrease in DL cell throughput and edge rates – a point also observed in [48]. However, when we increase the outage even more  $d_{\text{shift}} = 75\text{m}$ , we start to see that many UEs cannot establish a connection to any BS since the outage radius becomes comparable to the cell radius, which is 100 m. In other words, there is a non-zero probability that mobiles physically close to a cell may be in outage to that cell. These mobiles will need to connect to a much more distant cell. Therefore, we see the dramatic decrease in edge cell rate. Note that in our model, the front-to-back antenna gains are assumed to infinite, so mobiles that are blocked to one sector of a cell site cannot see any other sectors.

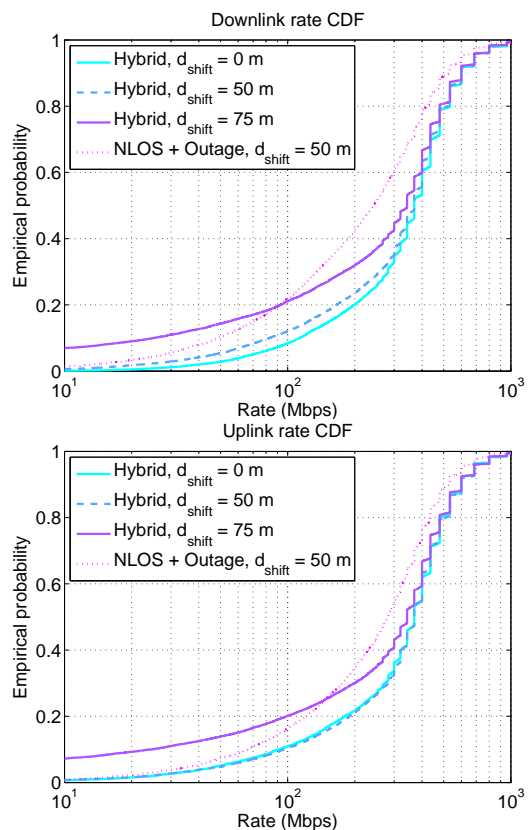


**Fig. 13:** Downlink (top plot) / uplink (bottom plot) rate CDF under the link state model with various parameters. The carrier frequency is 28 GHz.  $d_{\text{shift}}$  is the amount by which the outage curve in (8a) is shifted to the left.

Fig. 13 also shows that the throughputs are greatly benefited by the presence of LOS links. Removing the LOS links so that all links are in either an NLOS or outage states results in a significant drop in rate. However, even in this case, the mmW system offers a greater than 20 fold increase in rate over the comparison LTE system. It should be noted that the capacity numbers reported in [9], which were based on an

earlier version of this paper, did not include any LOS links.

We conclude that, in environments with outages condition similar to, or even somewhat worse than the NYC environment where our experiments were conducted, the system will be very robust to outages. This is extremely encouraging since signal outage is one of the key concerns for the feasibility of mmW cellular in urban environments. However, should outages be dramatically worse than the scenarios in our experiments (for example, if the outage radius is shifted by 75 m), many mobiles will indeed lose connectivity even when they are near a cell. In these circumstances, other techniques such as relaying, more dense cell placement or fallback to conventional frequencies will likely be needed. Such “near cell” outage will likely be present when mobiles are placed indoors, or when humans holding the mobile device block the paths to the cells. These factors were not considered in our measurements, where receivers were placed at outdoor locations with no obstructions near the cart containing the measurement equipment.

### CONCLUSIONS

We have provided the first detailed statistical mmW channel models for several of the key channel parameters including the path loss, and spatial characteristics and outage probability. The models are based on real experimental data collected in New York City in 28 and 73 GHz. The models reveal that signals at these frequencies can be detected at least 100 m to 200 m from the potential cell sites, even in absence of LOS connectivity. In fact, through building reflections, signals at many locations arrived with multiple path clusters to support spatial multiplexing and diversity.

Simple statistical models, similar to those in current cellular standards such as [25] provide a good fit to the observations. Cellular capacity evaluations based on these models predict an order of magnitude increase in capacity over current state-of-the-art 4G systems under reasonable assumptions on the antennas, bandwidth and beamforming. These findings provide strong evidence for the viability of small cell outdoor mmW systems even in challenging urban canyon environments such as New York City.

The most significant caveat in our analysis is the fact that the measurements, and the models derived from those measurements, are based on outdoor street-level locations. Typical urban cellular evaluations, however, place a large fraction of mobiles indoors, where mmW signals will likely not penetrate. Complete system evaluation with indoor mobiles will need further study. Also, indoor locations and other coverage holes may be served either via multihop relaying or fallback to conventional microwave cells and further study will be needed to quantify the performance of these systems.

### ACKNOWLEDGEMENTS

The authors would like to deeply thank several students and colleagues for providing the path loss data [19]–[22] that made this research possible: Yaniv Azar, Felix Gutierrez, DuckDong Hwang, Rimma Mayzus, George McCartney, Shuai Nie, Jocelyn K. Schulz, Kevin Wang, George N. Wong and Hang Zhao.

This work also benefitted significantly from discussions with our industrial partners in NYU WIRELESS program including Samsung, NSN, Qualcomm and InterDigital.

### REFERENCES

- [1] Cisco, “Cisco Visual Network Index: Global mobile traffic forecast update,” 2013.
- [2] Ericsson, “Traffic and market data report,” 2011.
- [3] UMTS Forum, “Mobile traffic forecasts: 2010-2020 report,” in *UMTS Forum Report*, vol. 44, 2011.
- [4] F. Khan and Z. Pi, “Millimeter-wave Mobile Broadband (MMB): Unleashing 3-300GHz Spectrum,” in *Proc. IEEE Sarnoff Symposium*, Mar. 2011.
- [5] —, “An introduction to millimeter-wave mobile broadband systems,” *IEEE Comm. Mag.*, vol. 49, no. 6, pp. 101 – 107, Jun. 2011.
- [6] T. S. Rappaport, J. N. Murdock, and F. Gutierrez, “State of the art in 60-GHz integrated circuits and systems for wireless communications,” *Proceedings of the IEEE*, vol. 99, no. 8, pp. 1390 – 1436, August 2011.
- [7] P. Pietraski, D. Britz, A. Roy, R. Pragada, and G. Charlton, “Millimeter wave and terahertz communications: Feasibility and challenges,” *ZTE Communications*, vol. 10, no. 4, pp. 3–12, Dec. 2012.
- [8] F. Boccardi, R. W. Heath, Jr., A. Lozano, T. L. Marzetta, and P. Popovski, “Five disruptive technology directions for 5G,” to appear in *IEEE Comm. Magazine*, 2014.
- [9] S. Rangan, T. S. Rappaport, and E. Erkip, “Millimeter-wave cellular wireless networks: Potentials and challenges,” *Proceedings of the IEEE*, vol. 102, no. 3, pp. 366–385, March 2014.
- [10] C. Doan, S. Emami, D. Sobel, A. Niknejad, and R. Brodersen, “Design considerations for 60 GHz CMOS radios,” *IEEE Comm. Mag.*, vol. 42, no. 12, pp. 132 – 140, 2004.
- [11] C. Doan, S. Emami, A. Niknejad, and R. Brodersen, “Millimeter-wave CMOS design,” *IEEE J. Solid-State Circuits*, vol. 40, no. 1, pp. 144–155, 2005.
- [12] Y.-P. Zhang and D. Liu, “Antenna-on-Chip and Antenna-in-Package solutions to highly integrated millimeter-wave devices for wireless communications,” *IEEE Trans. Antennas and Propagation*, vol. 57, no. 10, pp. 2830–2841, 2009.
- [13] F. Gutierrez, S. Agarwal, K. Parrish, and T. S. Rappaport, “On-chip integrated antenna structures in CMOS for 60 GHz WPAN systems,” *IEEE J. Sel. Areas Comm.*, vol. 27, no. 8, pp. 1367–1378, 2009.
- [14] J. Nsenga, A. Bourdoux, and F. Horlin, “Mixed analog/digital beamforming for 60 GHz MIMO frequency selective channels,” in *Proc. IEEE ICC*, 2010.
- [15] S. Rajagopal, S. Abu-Surra, Z. Pi, and F. Khan, “Antenna array design for multi-gbps mmwave mobile broadband communication,” in *Proc. IEEE Globecom*, 2011.
- [16] K.-C. Huang and D. J. Edwards, *Millimetre Wave Antennas for Gigabit Wireless Communications: A Practical Guide to Design and Analysis in a System Context*. Wiley Publishing, 2008.
- [17] F. Rusek, D. Persson, B. K. Lau, E. Larsson, T. Marzetta, O. Edfors, and F. Tufvesson, “Scaling up MIMO: Opportunities and challenges with very large arrays,” *IEEE Signal Process. Mag.*, vol. 30, no. 1, pp. 40–60, 2013.
- [18] T. S. Rappaport, *Wireless Communications: Principles and Practice*, 2nd ed. Upper Saddle River, NJ: Prentice Hall, 2002.
- [19] Y. Azar, G. N. Wong, K. Wang, R. Mayzus, J. K. Schulz, H. Zhao, F. Gutierrez, D. Hwang, and T. S. Rappaport, “28 GHz propagation measurements for outdoor cellular communications using steerable beam antennas in New York City,” in *Proc. IEEE ICC*, 2013.
- [20] H. Zhao, R. Mayzus, S. Sun, M. Samimi, J. K. Schulz, Y. Azar, K. Wang, G. N. Wong, F. Gutierrez, and T. S. Rappaport, “28 GHz millimeter wave cellular communication measurements for reflection and penetration loss in and around buildings in New York City,” in *Proc. IEEE ICC*, 2013.
- [21] M. K. Samimi, K. Wang, Y. Azar, G. N. Wong, R. Mayzus, H. Zhao, J. K. Schulz, S. Sun, F. Gutierrez, and T. S. Rappaport, “28 GHz angle of arrival and angle of departure analysis for outdoor cellular communications using steerable beam antennas in New York City,” in *Proc. IEEE VTC*, 2013.
- [22] T. S. Rappaport, S. Sun, R. Mayzus, H. Zhao, Y. Azar, K. Wang, G. N. Wong, J. K. Schulz, M. Samimi, and F. Gutierrez, “Millimeter wave mobile communications for 5G cellular: It will work!” *IEEE Access*, vol. 1, pp. 335–349, May 2013.

- [23] T. S. Rappaport, G. MacCartney, S. Sun, and S. Niu, "Wideband millimeter-wave propagation measurements and models for small cell, peer-to-peer, and backhaul wireless communications," Submitted to *IEEE JSAC Special Issue on 5G Cellular*, Dec. 2013.
- [24] S. Sun and T. S. Rappaport, "Multi-beam antenna combining for 28 GHz cellular link improvement in urban environments," in *Proc. IEEE Globecom*, Dec. 2013.
- [25] 3GPP, "Further advancements for E-UTRA physical layer aspects," TR 36.814 (release 9), 2010.
- [26] ITU, "M.2134: Requirements related to technical performance for IMT-Advanced radio interfaces," Technical Report, 2009.
- [27] M. R. Akdeniz, Y. Liu, S. Rangan, and E. Erkip, "Millimeter wave picocellular system evaluation for urban deployments," in *Globecom Workshops, 2013 IEEE*, Dec. 2013.
- [28] T. Zwick, T. Beukema, and H. Nam, "Wideband channel sounder with measurements and model for the 60 GHz indoor radio channel," *IEEE Trans. Vehicular Technology*, vol. 54, no. 4, pp. 1266–1277, July 2005.
- [29] F. Giannetti, M. Luise, and R. Reggiannini, "Mobile and personal communications in 60 GHz band: A survey," *Wireless Personal Communications*, vol. 10, pp. 207–243, 1999.
- [30] C. R. Anderson and T. S. Rappaport, "In-building wideband partition loss measurements at 2.5 and 60 GHz," *IEEE Trans. Wireless Comm.*, vol. 3, no. 3, pp. 922–928, May 2004.
- [31] P. Smulders and A. Wagemans, "Wideband indoor radio propagation measurements at 58 GHz," *Electronics Letters*, vol. 28, no. 13, pp. 1270–1272, June 1992.
- [32] T. Manabe, Y. Miura, and T. Ihara, "Effects of antenna directivity and polarization on indoor multipath propagation characteristics at 60 GHz," *IEEE J. Sel. Areas Comm.*, vol. 14, no. 3, pp. 441–448, April 1996.
- [33] E. Ben-Dor, T. S. Rappaport, Y. Qiao, and S. J. Lauffenburger, "Millimeter-wave 60 GHz outdoor and vehicle AOA propagation measurements using a broadband channel sounder," in *Proc. IEEE Globecom*, 2011, pp. 1–6.
- [34] H. Xu, V. Kukshya, and T. S. Rappaport, "Spatial and temporal characteristics of 60 GHz indoor channel," *IEEE J. Sel. Areas Comm.*, vol. 20, no. 3, pp. 620–630, April 2002.
- [35] H. Zhang, S. Venkateswaran, and U. Madhow, "Channel modeling and MIMO capacity for outdoor millimeter wave links," in *Proc. IEEE WCNC*, April 2010.
- [36] S. Akoum, O. E. Ayach, and R. W. Heath, Jr., "Coverage and capacity in mmWave cellular systems," in *Proc. of Asilomar Conf. on Signals, Syst. & Computers*, Pacific Grove, CA, Nov. 2012.
- [37] A. Elrefaie and M. Shakouri, "Propagation measurements at 28 GHz for coverage evaluation of local multipoint distribution service," *Proc. Wireless Communications Conference*, pp. 12–17, Aug. 1997.
- [38] S. Seidel and H. Arnold, "Propagation measurements at 28 GHz to investigate the performance of Local Multipoint Distribution Service (LMDS)," *Proc. Wireless Communications Conference*, pp. 754–757, Nov. 1995.
- [39] T. S. Rappaport, F. Gutierrez, E. Ben-Dor, J. N. Murdock, Y. Qiao, and J. I. Tamir, "Broadband millimeter-wave propagation measurements and models using adaptive-beam antennas for outdoor urban cellular communications," *IEEE Trans. Antennas and Propagation*, vol. 61, no. 4, pp. 1850–1859, 2013.
- [40] T. S. Rappaport, E. Ben-Dor, J. Murdock, and Y. Qiao, "38 GHz and 60 GHz angle-dependent propagation for cellular and peer-to-peer wireless communications," *Proc. IEEE ICC*, pp. 4568–4573, Jun. 2012.
- [41] T. S. Rappaport, E. Ben-Dor, J. Murdock, Y. Qiao, and J. Tamir, "Cellular broadband millimeter wave propagation and angle of arrival for adaptive beam steering systems," in *Proc. IEEE RWS (Invited)*, Jan. 2012.
- [42] J. Murdock, E. Ben-Dor, Y. Qiao, J. Tamir, and T. S. Rappaport, "A 38 GHz cellular outage study for an urban outdoor campus environment," in *Proc. IEEE WCNC*, April 2012.
- [43] G. R. MacCartney, Jr., J. Zhang, S. Nie, and T. S. Rappaport, "Path loss models for 5G millimeter wave propagation channels in urban microcells," in *Proc. IEEE Globecom*, Dec. 2013.
- [44] J. A. Wells, "Faster than fiber: The future of multi-Gb/s wireless," *IEEE Microwave Magazine*, vol. 10, no. 3, pp. 104–112, May 2009.
- [45] C. M. Bishop, *Pattern Recognition and Machine Learning*, ser. Information Science and Statistics. New York, NY: Springer, 2006.
- [46] P. Kyösti, J. Meinilä, L. Hentilä, X. Zhao, T. Jämsä, M. Narandzic, M. Milojevic, C. Schneider, A. Hong, J. Ylitalo, V.-M. Holappa, M. Alatosava, R. Bultitude, Y. de Jong, and T. Rautiainen, "WINNER II channel models part II radio channel measurement and analysis results," IST-4-027756 WINNER II D1.1.2 V1.0, 2007.
- [47] T. Bai and R. W. Heath, Jr., "Coverage and rate analysis for millimeter wave cellular networks," arXiv:1402.6430v2 [cs.IT], Mar. 2014.
- [48] T. Bai, R. Vaze, and R. W. Heath Jr., "Analysis of blockage effects on urban cellular networks," arXiv preprint arXiv:1309.4141, Sep. 2013.
- [49] S. Nie, G. R. MacCartney, Jr., S. Sun, and T. S. Rappaport, "28 GHz and 73 GHz signal outage study for millimeter wave cellular and backhaul communications," in *Proc. IEEE ICC*, Jun. 2014, to appear.
- [50] D. Tse and P. Viswanath, *Fundamentals of Wireless Communication*. Cambridge University Press, 2007.
- [51] A. Alkhateeb, O. E. Ayach, G. Leus, and R. W. Heath, Jr., "Hybrid precoding for millimeter wave cellular systems with partial channel knowledge," in *Proc. Information Theory and Applications Workshop (ITA)*, Feb. 2013.
- [52] D. Parker and D. Z. Zimmermann, "Phased arrays-part I: Theory and architecture," *IEEE Trans. Microw. Theory Tech.*, vol. 50, no. 3, pp. 678–687, Mar. 2002.
- [53] K.-J. Koh and G. M. Rebeiz, "0.13- $\mu\text{m}$  CMOS phase shifters for X-, Ku- and K-band phased arrays," *IEEE J. Solid-State Circuits*, vol. 42, no. 11, pp. 2535–2546, Nov. 2007.
- [54] —, "A millimeter-wave (40–45 GHz) 16-element phased-array transmitter in 0.18- $\mu\text{m}$  SiGe BiCMOS technology," *IEEE J. Solid-State Circuits*, vol. 44, no. 5, pp. 1498–1509, May 2009.
- [55] P. E. Crane, "Phased array scanning system," United States Patent 4,731,614, filed Aug 11, 1986, issued Mar. 15, 1988.
- [56] S. Raman, N. S. Barker, and G. M. Rebeiz, "A W-band dielectric lens-based integrated monopulse radar receiver," *IEEE Trans. Microw. Theory Tech.*, vol. 46, no. 12, pp. 2308–2316, Dec. 1998.
- [57] X. Guan, H. Hashemi, and A. Hajimiri, "A fully integrated 24-GHz eight-element phased-array receiver in silicon," *IEEE J. Solid-State Circuits*, vol. 39, no. 12, pp. 2311–2320, Dec. 2004.
- [58] A. Lozano, "Long-term transmit beamforming for wireless multicasting," in *Proc. ICASSP*, vol. 3, 2007, pp. III–417–III–420.
- [59] J. P. Kermaol, L. Schumacher, K. I. Pedersen, P. E. Mogensen, and F. Frederiksen, "A stochastic MIMO radio channel model with experimental validation," *IEEE J. Sel. Areas Comm.*, vol. 20, no. 6, pp. 1211–1226, 2002.
- [60] D. McNamara, M. Beach, and P. Fletcher, "Spatial correlation in indoor MIMO channels," in *Proc. IEEE PIMRC*, vol. 1, 2002, pp. 290–294.
- [61] S. Pinel, S. Sarkar, P. Sen, B. Perumana, D. Yeh, D. Dawn, and J. Laskar, "A 90nm CMOS 60 GHz Radio," in *Proc. IEEE International Solid-State Circuits Conference*, 2008.
- [62] C. Marcu, D. Chowdhury, C. Thakkar, J.-D. Park, L.-K. Kong, M. Tabesh, Y. Wang, B. Afshar, A. Gupta, A. Arbabian, S. Gambini, R. Zamani, E. Alon, and A. Niknejad, "A 90 nm CMOS low-power 60 GHz transceiver with integrated baseband circuitry," *IEEE J. Solid-State Circuits*, vol. 44, pp. 3434–3447, 2009.
- [63] P. Mogensen, W. Na, I. Z. Kovács, F. Frederiksen, A. Pokhariyal, K. I. Pedersen, T. Kolding, K. Hugel, and M. Kuusela, "LTE capacity compared to the Shannon bound," in *Proc. IEEE VTC*, 2007.
- [64] J. C. Ikuno, C. Mehlfuhrer, and M. Rupp, "A novel link error prediction model for OFDM systems with HARQ," in *Proc. IEEE ICC*, 2011.